# Magnetic resonance imaging of sea-ice pore fluids: methods and thermal evolution of pore microstructure

H. Eicken [a,*], C. Bock [b], R. Wittig [b], H. Miller [b], H.-O. Poertner [b]

[a] *Geophysical Institute, University of Alaska Fairbanks, P.O. Box 757320, Fairbanks, AK 99775-7320, USA*
[b] *Alfred Wegener Institute for Polar and Marine Research, P.O. Box 120161, D-27515 Bremerhaven, Germany*

## Abstract

Microstructure and thermal evolution of sea-ice brine inclusions were investigated with magnetic resonance imaging (MRI) techniques. Ice samples were kept at temperatures between $-2°C$ and $-25°C$ during ^{1}H imaging in a 4.7-T magnet at 200 MHz. Measurements were completed in a 20-cm diameter cylindrical probe and actively shielded gradient coils (max. 50 mT m$^{-1}$, pixel dimensions > 0.2 mm, slice thicknesses > 1 mm), and for higher resolution in a mini-imaging unit with a 9-cm diameter probe with gradient coils of 200 mT m$^{-1}$ (pixel dimensions < 0.1 mm, slice thickness < 0.4 mm). Absorption of radio-frequency (RF) signals in the dielectrically lossy brine resulted in degraded signals and was alleviated by use of a contrast agent (decane). MRI data and sea-ice thin section images agree very well (< 5% deviation for pore microstructural parameters). Analysis of ice grown under different current speeds indicates that pores are smaller and pore number densities larger at higher current speeds. The thermal evolution of fluid inclusions was studied on cold first-year ice samples, maintained at close to in-situ temperatures prior to experiments. Warming from $-21°C$ to $-10°C$ to $-6°C$ is associated with a distinct increase in pore size (from 1.5 to 1.7 to 2.6 mm for the upper 10-percentile in the vertical) and elongation (4.0 to 4.2 to 6.2 for ratio of major to minor pore axes in the vertical) and a decrease in number densities (0.75 to 0.62 to 0.58 mm$^{-3}$ in the vertical). Aspect ratios increased from 4:2:1 to 6:2:1 (upper 10-percentile), indicating expansion and merging of pores in the vertical, possibly promoted by microscopic residual brine inclusions. © 2000 Elsevier Science B.V. All rights reserved.

*Keywords:* Sea ice; Nuclear magnetic resonance; Pore structure; Crystal growth; Chukchi Sea; Image analysis

## 1. Introduction

Sea ice is distinct from other types of ice present at the earth's surface owing to the ubiquitous occurrence of sub-millimeter to decimeter-sized inclusions of liquid brine (Weeks and Ackley, 1986; Weeks, 1998; Wettlaufer, 1998). These inclusions strongly affect radiative and heat transfer through the ice (Perovich, 1998; Weeks, 1998) and they control the electromagnetic properties of sea ice (Hallikainen and Winebrenner, 1992; Golden et al., 1998a,b). As the brine seeks to maintain thermodynamic equilibrium with the ice matrix, the morphology and size of the inclusions depends strongly on the salinity and

* Corresponding author. Fax: +1-907-474-7290.
  *E-mail address:* hajo.eicken@gi.alaska.edu (H. Eicken).

have been maintained at the in-situ temperature after sampling. The ice samples originate both from ice-tank experiments devoted to the study of microstructural evolution (Eicken et al., 1998) as well as from coastal sea ice obtained at Barrow in northern Alaska. Apart from a discussion of methodological aspects, the evolution of pore microstructure will receive particular attention in the context of ice permeability and fluid transport at lower temperatures (Golden et al., 1998a,b; Freitag, 1999), as the present contribution is part of a study devoted to fluid transport and its importance for survival of microorganisms within sea-ice pores at low temperatures (Eicken et al., 1999; Deming and Huston, in press; Junge et al., in press).

## 2. Methods

### 2.1. Principles and instrumentation of MRI

The detection of water within a multi-phase system with nuclear magnetic resonance (NMR) techniques is a well-established technique and among other topics has also been applied to problems in sea-ice research to study the thermal evolution of the brine fraction in sea ice (Richardson and Keller, 1966; Richardson, 1976; Melnichenko et al., 1979). MRI is based on the principle that the resonance frequency depends on the position of a nucleus in a magnetic field gradient (Wehrli, 1988; Callaghan, 1991). The frequency spectrum obtained over a sample volume can then be decomposed into individual frequencies (containing information about the $x$–$y$ position) and amplitudes (containing information about the spin, or in the case of $^1H$, proton density). Image acquisition and in particular the spatial resolution are determined by the timing and characteristics of the RF pulses as well as the magnitude of the field gradient across the sample volume.

The present study has been carried out in a Bruker Biospec 47/40 imaging spectrometer (Bruker, Ettlingen, Germany), at 4.7 T (Larmor frequency for $^1H$ = 200 MHz) equipped with actively shielded gradient coils providing field gradients of 50 mT m$^{-1}$ and a mini-imaging unit with gradient field strength of up to 200 mT m$^{-1}$. Cylindrical probes adapted to

high-conductivity samples were used for RF signal transmission and detection (20- and 9-cm diameter, respectively). Image acquisition was mostly confined to a spin–echo method (multi-slice multi-echo, MSME, matrix size up to 1024 × 512, field-of-view (FOV) up to 12 × 12 cm (standard imaging, S) or 6 × 6 cm (mini imaging, M), slice thickness down to 1.2 mm (S) or 0.3 mm (M), slice separation down to 5 mm (S) or 2 mm (M), with sinc3 RF pulses of 3000-$\mu$s duration) or a gradient–echo method (FLASH, flip angle 22.5°, sinc3 of 3000 $\mu$s) with typical echo times TE of 17.5 ms for MSME and 5 ms for FLASH. Repetition time TR was on the order of 300–2000 ms for MSME and 400–500 ms for FLASH. Typically, measurements for individual samples lasted between 4 and 12 h, averaging over up to eight samples in order to increase the signal-to-noise ratio (SNR).

### 2.2. Samples and sample preparation

In order to optimize MRI system performance and to develop and improve upon methods of MRI data analysis, a first set of measurements was carried out on artificial sea ice grown under fully controlled environmental conditions. These samples originated from ice-growth experiments in the Environmental Arctic Test Basin (EATB) of the Hamburgische Schiffbauversuchsanstalt in 1996 and 1997 (INTERICE I, Eicken et al., 1998). In a basin of dimensions 30 × 6 × 1.2 m, a congelation-type sea-ice sheet was grown from artificial seawater, prepared by dissolving Aquarium Systems "Instant Ocean" artificial seasalt in tapwater, to between 0.15- and 0.2-m thickness (for details, see Eicken et al., 1998). The resulting ice is representative of new ice grown under natural conditions and exhibits the same inventory of small- and large-scale pore features (Cottier et al., 1999; Eicken et al., in preparation).

Samples for the studies of sea-ice thermal evolution were obtained in March 1999 from the fast-ice cover near Barrow (sampling location at 71°19.95′N 156°40.55′W), on the northern coast of Alaska. Numerous studies of the ice cover at this location have shown it to be representative of homogeneous first-year, undeformed Arctic congelation-type sea ice (Weeks and Gow, 1978; Cole and Shapiro, 1998). At

physical properties and microstructure of the sample. Given the lack of sea-ice MRI work, a first step in the present study consisted of an optimization of the instrumental parameters. Analysis of ice samples immersed in brine at the respective in-situ temperatures established that the SNR of gradient–echo FLASH images was poor, most likely due to RF loss in the brine, and that the images showed artifacts due to susceptibility changes within the ice matrix (resulting from air bubbles, brine–ice transitions, eddy currents). Spin–echo images yielded results that were not severely compromised by artifacts due to eddy currents induced in the brine layer surrounding the sample (5- to 10-mm thick, see bottom of Fig. 2).
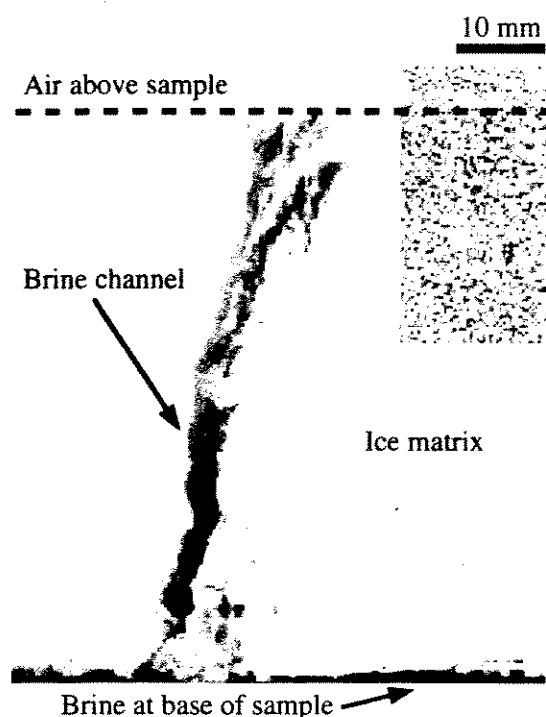


Fig. 2. MRI cross-section through layer of artificial sea ice (sample H961219Q, 0.07- to 0.14-m depth, slice thickness 1.5 mm, pixel size 0.4×0.4 mm) recorded in immersion of artificial brine at −2°C with a spin–echo method (MSME). Note that here and in all subsequent images, MRI and thin-section scenes are shown as inverted contrast images (pores appearing dark). While the brine channel in the center is well discernible, very few pore features can be identified in the ice matrix, as is evident from the subregion in the upper right that has been subjected to a linear histogram transform to enhance the contrast in the ice matrix.

However, due to the higher RF power input (90°–180° flip angles) in comparison to FLASH, the probe was heating up at in-situ temperatures, compromising long-term image sampling. As apparent from the vertical cross-section through a new-ice cover shown in Fig. 2, the structure of brine channels and other larger pore features is well-resolved. This includes the upper layers of the sample where the channel is widened and to some extent branched out. As shown by the contrast-enhanced inset in Fig. 2, there is no discernible difference in the signal between ice matrix and overlying air. At a pixel size of approximately 0.4 mm and a slice thickness of 1.5 mm, smaller brine inclusions are not distinguishable within the ice matrix.

While the resolution of the imaging system as defined by the size of the volume elements (voxels) may not allow for direct discrimination of small-scale pores, it can still be feasible to derive the fraction of such fluid inclusions based on the signal strength integrated over a larger sample sub-volume. Based on Callaghan (1991), the SNR for a signal induced in the receiver coils of radius $r$ during resonance at frequency $f_0$ and for a frequency bandwidth $\Delta f$ is directly proportional to the volume fraction $N_p$ of protons (in this case ^{1}H in the brine) in a subvolume $V_s$ such that

$$\mathrm{SNR} \approx K \frac{N_p V_s f_0^{7/4}}{r \Delta f^{1/2}} \tag{1}$$

with constant $K = 1.2 \times 10^{-3}$ s$^{5/4}$ m$^{-2}$ based on instrument parameters and assuming solenoidal coils at room temperature. For a voxel volume of (0.4 mm)$^3$ and parameters characteristic of the Bruker system employed in this study, SNR is roughly 100 in order of magnitude, with values decreasing to below 10 as higher resolutions are approached. In solids, the signal is broadened over a wider resonance frequency band. In combination with shorter relaxation times this allows for a direct discrimination between brine and ice, with the signal for pure ice and air being close to indistinguishable (Fig. 2, Table 1). Disregarding the submicroscopic effects on the relaxation of ^{1}H along phase boundaries, the liquid fraction $f_s$ in a given sample volume with a signal of magnitude $S$ can be derived through a set
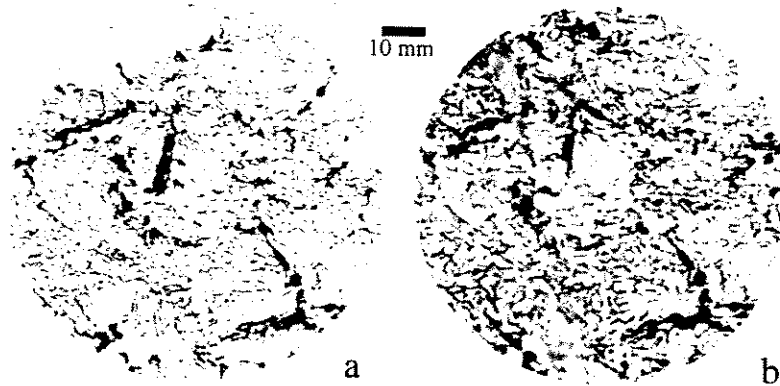
Fig. 3. Comparison of pore microstructure between horizontal thin-section image (a) and MRI data (b) of the same sea-ice sample (H961219Q, 0.05-m depth). Pores appear dark in both images, with both larger secondary brine channels and pockets as well as smaller brine layers discernible. Pore-free areas along margin of upper half of thin-section sample are artifacts due to sample processing (see Table 2 for further details on image acquisition and data).

ton density as well as its immiscibility with water. In this way, spin–echo imaging could be performed with greater matrix sizes to increase resolution, more adequate and shorter pulses resulting in thinner slice thicknesses, and a larger number of signal averages to increase SNR. At the same time, RF heating was significantly reduced due to better probe matching and reduction in eddy currents, allowing for longer measurement periods. Fig. 3 demonstrates that samples saturated with decane resulted in a significant improvement of image quality. Moreover, increased signal strength allowed for a reduction in the linear voxel dimensions by more than half (see instrument parameters shown in Table 2). Thus, in a standard mode of operation with a field gradient of 50 mT

m$^{-1}$ in the 20-cm-diameter resonator, the method appears to sufficiently resolve both larger-scale pores such as brine channels as well as the sub-millimeter brine layers characteristic of columnar sea ice (Fig. 3).

### 3.2. Segmentation of MRI data

Quantitative microstructural analysis requires the segmentation of MRI data into solid ice and fluid inclusions. In the case of MRI this can be approached in a rigorous fashion, given that the signal is proportional to the total number of liquid-phase protons in a given sub-volume. Hence, the signal associated with the pure end-member components $S_s$ and $S_l$ (ice and brine or decane) can be employed to constrain Eq. (2) and allow for the derivation of the liquid volume fraction (i.e., porosity) of individual volume elements. $S_s$ and $S_l$ can be derived either manually through measurement over a test volume or from a sample histogram such as the one shown in Fig. 4. With the liquid volume fraction computed from the signal of each individual voxel according to Eq. (2), the segmentation criterion can be based on a simple fractional-volume threshold, with all voxels corresponding to a liquid volume fraction $f_l \leq 0.5$ classified as ice and all those with $f_l > 0.5$ as pores. The classification error due to a finite SNR can then be derived from the FOV and the number of samples averaged for each data set (see Section 5.1).

Table 2

Comparison between thin-section image and MRI data (sample H961219Q, 0.05-m depth, low-resolution standard gradient coils, see Fig. 3)

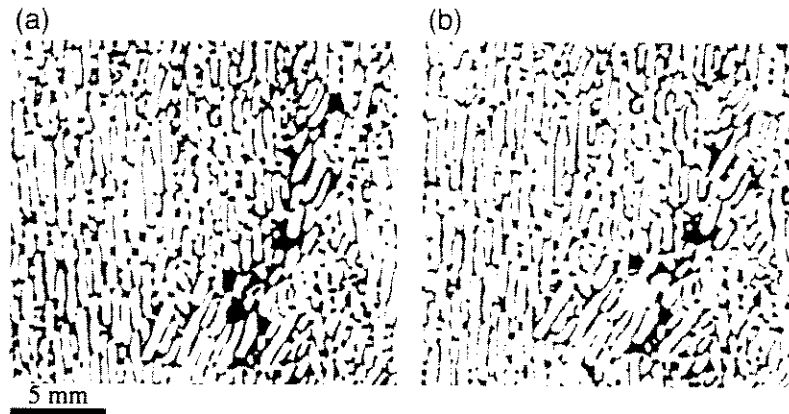| Parameter | Thin section data | MRI data |
|---|---|---|
| | Mean ± $\sigma$ | Mean ± $\sigma$ |
| Pixel size (horizontal), mm | 0.18 | 0.21 |
| Slice thickness (vertical), mm | < 0.05 | 1.26 |
| Porosity | 0.187 | 0.176 |
| Pore area, mm$^2$ | 0.76 ± 3.40 | 1.10 ± 4.40 |
| Pore perimeter, mm | 3.34 ± 7.40 | 3.97 ± 8.60 |
| Pore major axis, mm | 1.06 ± 1.23 | 1.19 ± 1.44 |
| Pore minor axis, mm | 0.45 ± 0.44 | 0.58 ± 0.56 |

Fig. 6. Comparison of pore microstructure between horizontal thin-section image (a) — averaged over three serial sections spaced 0.2 mm apart — and MRI data recorded with the mini-imaging unit (b) of the same sea-ice sample (H970128Q, 0.15-m depth). Pores appear dark in both images, with system of subparallel brine layers clearly discernible (see Table 3 for further details on image acquisition and pore-size data).

Ackley, 1986). With an FOV extending over close to 100 mm, a pixel resolution of around 0.2 mm and a slice thickness of > 1 mm (Table 2), imaging in a field gradient of 50 mT m$^{-1}$ is ideal for studies of pore macrostructure in a larger sample volume (Figs. 2 and 3), but proved only marginally effective at properly resolving the sub-millimeter pore structure. This is also borne out by the mismatch apparent between thin-section and MRI data at smaller pore sizes in Fig. 5.

A significant increase in resolution and data quality has been achieved, however, by imaging in higher field gradients of up to 200 mT m$^{-1}$. In combination with the cooling chamber, this system allows for the

analysis of samples with approximate dimensions 30 × 30 × 60 mm, comparable to high-resolution image analysis of thin sections. While the smaller FOV reduces the SNR, this can be compensated for by longer integration times. Smaller sample sizes also reduce the amount of attenuation of the RF signal

Table 3
Comparison between thin-section image and MRI data (sample H970128Q, 0.15-m depth, high-resolution, 200 mT m$^{-1}$ gradient coils, see Fig. 6)

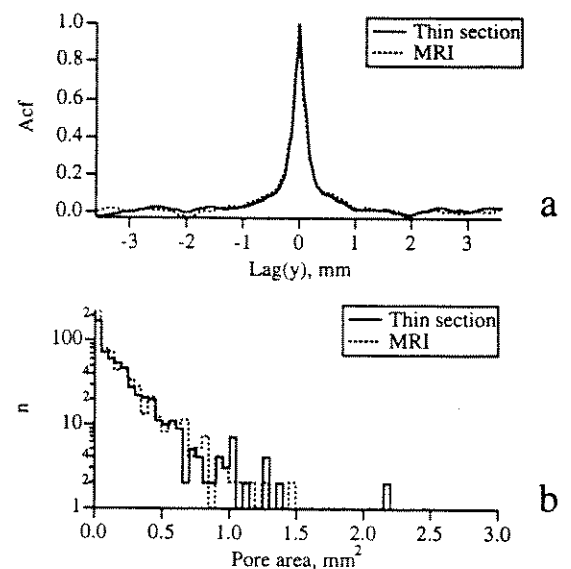| Parameter | Thin section data | MRI data |
|---|---|---|
| | Mean $\pm \sigma$ | Mean $\pm \sigma$ |
| Pixel size (horizontal), mm | 0.08 | 0.09 |
| Slice thickness (vertical), mm | < 0.05 | 0.4 |
| Porosity | 0.175 | 0.181 |
| Pore area, mm$^2$ | 0.32 ± 1.31 | 0.28 ± 0.66 |
| Pore perimeter, mm | 2.92 ± 5.80 | 2.72 ± 3.93 |
| Pore major axis, mm | 0.87 ± 0.90 | 0.85 ± 0.82 |
| Pore minor axis, mm | 0.30 ± 0.23 | 0.29 ± 0.22 |



Fig. 7. Comparison of microstructural parameters for thin-section and MRI images shown in Fig. 6 (sample H970128Q, 0.15-m depth). Vertical cross-section through 2-D acf (Fig. 7a) and pore-size distribution based on cross-sectional pore area (Fig. 7b).

Table 4

Comparison between MRI data (horizontal and vertical sections) for ice grown at different under-ice current speeds (high-resolution imaging at 200 mT m$^{-1}$, see Figs. 8 and 9; mean and standard deviation for mean values of eight individual sections per sample are shown)

| Parameter | H970128Q, 0.15 m | | H961219C, 0.08 m | |
|---|---|---|---|---|
| | Horizontal | Vertical | Horizontal | Vertical |
| Current velocity, m s$^{-1}$ | 0.00 | 0.00 | 0.16 | 0.16 |
| Porosity | 0.21 ± 0.01 | 0.20 ± 0.02 | 0.11 ± 0.01 | 0.11 ± 0.01 |
| Pore area, mm$^2$ | 0.27 ± 0.03 | 0.43 ± 0.10 | 0.14 ± 0.02 | 0.25 ± 0.04 |
| Pore perimeter, mm | 2.66 ± 0.26 | 2.94 ± 0.47 | 1.43 ± 0.11 | 1.95 ± 0.15 |
| Pore major axis $a_{maj}$, mm | 0.83 ± 0.06 | 0.87 ± 0.13 | 0.50 ± 0.03 | 0.68 ± 0.03 |
| Pore minor axis $a_{min}$, mm | 0.30 ± 0.02 | 0.30 ± 0.03 | 0.24 ± 0.01 | 0.25 ± 0.01 |

tions with an under-ice current speed of approximately 0.16 m s$^{-1}$. These measurements are motivated by the lack of data and understanding of the microstructural evolution of sea ice in different hydrodynamic regimes in particular as it relates to pore structure and ice properties. Changes in the microstructural evolution are forced by variability in the thickness and structure of the laminar boundary layer, on the order of a few millimeters thick, ahead of the advancing ice–water interface (Weeks and Ackley, 1986; Wettlaufer, 1998). The MRI data presented here are complementary to a more detailed study of the evolution of pore space as a function of under-ice current speed based mostly on horizontal thin-section data by Eicken et al. (in preparation).

A comparison between the image data shown for an ice cover grown at zero current (Fig. 8) and at an under-ice current speed of approximately 0.16 m s$^{-1}$ (Fig. 9), in the upper range of natural conditions (McPhee, 1990), demonstrates strong contrasts in microstructure. For ice affected by a current of this magnitude, the grain substructure with parallel or sub-parallel brine layers separated by orderly arrays of ice lamellae (Fig. 8a) breaks down into smaller disjoint pores of more isometric cross-section (Fig. 9a). In the vertical plane (Figs. 8b and 9b), this structural change is just as pronounced with the parallel brine layer arrays replaced by shorter (Fig. 9c), less well-ordered brine tubes. Such changes evident in the MRI scenes are reflected in the pore-
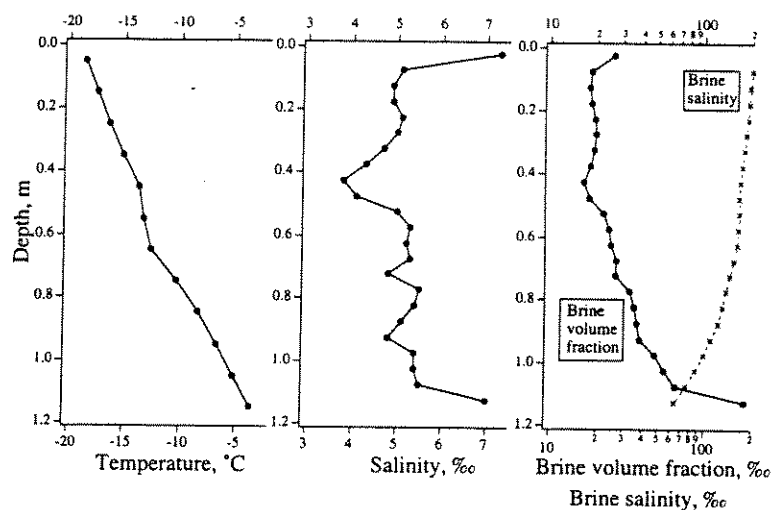


Fig. 10. Profiles of temperature (left), salinity (center) as well as brine volume fraction and brine salinity (right, derived based on phase relations according to Cox and Weeks, 1983) through the fast-ice sheet at the sampling site near Barrow in the Chukchi Sea (March 12, 1999).

fluid inclusions cannot be arrived at in such a fashion, however. The few observations of changes in pore structure are either based on semi-quantitative microscopy (Assur, 1960) or measurements carried out on larger populations of samples (Perovich and Gow, 1996).

Here, we have studied changes in pore microstructure associated with a warming from below −21°C to −6°C throughout the same, undisturbed ice sample volume. Samples had been obtained from the coastal fast-ice cover in the eastern Chukchi Sea near Barrow during the coldest weeks of the year (Section 2.2). Temperatures were maintained at or close to the in-situ temperature which approached −20°C in the upper ice layers (Fig. 10) up to the start of the MRI analysis. Salinity measurements and microstructural studies performed on additional ice cores obtained at the study site indicate the ice cover to consist of prototypical first-year columnar, congelation-type sea ice with a C-shaped salinity profile

(Figs. 10 and 11), which is in agreement with earlier studies carried out at this location (Weeks and Gow, 1978; Cole and Shapiro, 1998). The MRI sample was obtained from the cold, uppermost layers of columnar ice, composed of smaller crystals and lacking the preferred azimuthal alignment of crystallographic c-axes displayed at greater depths (Fig. 11). Based on the salinity and temperature measurements, the brine volume fraction in the upper layers of columnar sea ice is approximately 20‰ (Fig. 10, derived according to Cox and Weeks, 1983). The corresponding MRI data shown in Fig. 12 and Table 5 are in fair agreement with this bulk brine porosity.

The most interesting aspects of Fig. 12, however, are the changes in pore microstructure associated with a warming of the sample from −21°C to −6°C. As is clearly evident, pores present at low temperatures enlarge and join, while at the same time new populations of pores appear in the image data (see Table 5, pore number densities). The latter are

Table 5

Thermal evolution of pore microstructural parameters as derived from MRI data for sample CS990312, 0.10- to 0.13-m depth (bold numbers in upper rows are mean values, standard deviation indicated in lower rows)

| $T$ (°C) | Vertical sections | | | Horizontal sections | | | $P$ | $N_{P,ver}$ (mm$^{-3}$) | $N_{P,hor}$ (mm$^{-3}$) |
|---|---|---|---|---|---|---|---|---|---|
| | $a_{maj}$ (mm) | $a_{min}$ (mm) | $r_{maj/min}$ | $a_{maj}$ (mm) | $a_{min}$ (mm) | $r_{maj/min}$ | | | |
| *Entire data set* | | | | | | | | | |
| −21 | **0.42** | **0.21** | **1.73** | **0.34** | **0.22** | **1.49** | **0.026** | **0.75** | **0.95** |
| | 0.47 | 0.10 | 1.10 | 0.19 | 0.09 | 0.56 | | | |
| *Top 10 percentile* | | | | | | | | | |
| −21 | **1.53** | **0.40** | **3.96** | **0.75** | **0.37** | **2.16** | | | |
| | 0.70 | 0.11 | 1.61 | 0.23 | 0.10 | 0.87 | | | |
| *Entire data set* | | | | | | | | | |
| −10 | **0.43** | **0.22** | **1.73** | **0.34** | **0.23** | **1.46** | **0.027** | **0.62** | **1.05** |
| | 0.52 | 0.10 | 1.18 | 0.22 | 0.10 | 0.57 | | | |
| *Top 10 percentile* | | | | | | | | | |
| −10 | **1.66** | **0.40** | **4.20** | **0.81** | **0.39** | **2.19** | | | |
| | 0.83 | 0.10 | 1.89 | 0.33 | 0.10 | 0.88 | | | |
| *Entire data set* | | | | | | | | | |
| −6 | **0.70** | **0.26** | **2.32** | **0.38** | **0.25** | **1.53** | **0.038** | **0.58** | **1.08** |
| | 0.79 | 0.13 | 1.74 | 0.24 | 0.11 | 0.59 | | | |
| *Top 10 percentile* | | | | | | | | | |
| −6 | **2.62** | **0.45** | **6.16** | **0.92** | **0.42** | **2.32** | | | |
| | 1.06 | 0.15 | 2.37 | 0.34 | 0.12 | 0.84 | | | |

$a_{maj}$, $a_{min}$: major and minor axis of inscribed ellipse, $r_{maj/min}$: ratio between major and minor axis, $P$: porosity, $N_{P,ver}$, $N_{P,hor}$: number density of pores.

incident light, is the slice thickness, which may be larger than the characteristic pore dimension. Slice thicknesses for MRI data measured with the standard gradient coils are generally larger than 1 mm (depending on matrix size, FOV and available RF power) and even a data set optimized for resolution is likely to have slice thicknesses larger than 0.3 mm. This introduces stereological effects (Underwood, 1970; Eicken, 1993) that affect the apparent pore size and to a lesser extent, for columnar sea ice, the apparent shape of the inclusions.

The close spacing between individual slices, such as a set of eight separated by approximately 4 mm each for the samples shown in Figs. 8 and 9, allows an assessment of the spatial variability of pore volume and microstructure at a very small scale. The standard deviation of the slice porosities varies between 7% and 12% for these two different samples (Table 4), with maximum deviations of 20%, corresponding to maximum bulk salinity differences of approximately 1.4‰ salinity. Microstructural size parameters also exhibit standard deviations of 5–10% between sets of horizontal or vertical slices. These fluctuations are most likely associated with grain-boundaries and other microstructural discontinuities in the sample.

## 5.2. The thermal evolution of sea-ice pore space

In contrast with destructive imaging techniques such as standard thin-section processing, MRI can provide imagery of a larger sea-ice sample as it undergoes temperature changes. Here, these changes have been documented for a sample of columnar ice maintained close to in-situ temperatures after coring and then warmed from $-21°C$ to $-6°C$. As shown in Fig. 12 and Table 5 and summarized in Fig. 13, warming was accompanied by significant microstructural changes, in particular between $-10°C$ and $-6°C$. Concurrently, pore volumes increased by approximately 50%, which is in good agreement with theoretical estimates based on the ice salinity and thermodynamic phase relations (Fig. 13). As expected, based on earlier semi-quantitative observations on thin sections (Assur, 1960, Weeks and Ackley, 1986), the vertical elongation of pores increases as a result of warming, with the ratio between major and minor axis (inscribed ellipse)
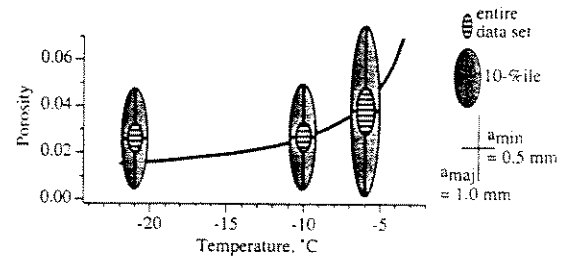


Fig. 13. Thermal evolution of fluid inclusions for Chukchi Sea ice sample (CS990312, 0.13- to 0.16-m depth, see Fig. 10 for profile properties and Fig. 11 for thin-section images) based on MRI data. The relative proportions of the major and minor pore axis dimensions are shown for the entire data set and the upper 10-percentile (scale shown at right). The solid line denotes the increase in brine porosity based on sample bulk salinity and phase relations.

$r_{maj/min}$ increasing from 4 to more than 6 for the upper 10-percentile of pores in a sample. During the same temperature interval, $r_{maj/min}$ increased by less than 10% to 2.3% for the upper 10-percentile in horizontal MRI slices. Based on the mean parameters, the aspect ratios of brine inclusions in three dimensions (vertical, horizontal parallel to crystal basal layer, horizontal perpendicular to basal layer) have thus been observed to increase from 1.9:1.5:1 to 2.8:1.5:1 for the entire pore population and from 4.1:2.0:1 to 6.2:2.2:1 for the upper 10-percentile.

With increasing size, pores have been observed to merge and coalesce (Fig. 14). While this circumstance is also reflected in a decrease in the number density of pores $N_p$ in vertical MRI slices, the appearance of new populations of small pores in the image data has diminished the overall magnitude of this effect. Fig. 14 illustrates the problem and also shows that the assessment of pore morphology (e.g., $r_{maj/min}$) is to some extent compromised as well. Thus, the merging of four apparently isolated pores into a large, tubular inclusion in the center is accompanied by the "appearance" of new pores to the right and above this major feature. The latter are responsible for an increase in $N_p$ for this small sub-scene. In the horizontal MRI slices, this process is believed to be responsible for the slight increase observed for $N_{p,hor}$ with increasing temperature (Table 5). A similar, and upon first reflection counter-intuitive trend was reported by Perovich and Gow (1996) in their analysis of thin-section images of warming ice sam-

Finally, the issue of resolution also affects interpretation of MRI data in the context of pore connectivity and fluid transport. Thus, the interpretation of the merging of individual pores discussed above and shown in Fig. 14 only applies to pore connections visible at the smallest scale resolved in the data set. At sub-pixel scales, the set of pores barely discernible at −21°C in Fig. 14 may already have been linked through smaller-scale vein networks. Given some of the limitations of both MRI and ordinary thin-section analysis, we suspect that only true microscopic analysis may provide deeper insight into this problem. The relevance of this question far exceeds the merely technical aspects of microstructural analysis, however. While the finding that pores are preferentially elongating and in particular merging in the vertical direction is compatible with classical sea-ice pore microstructural models, all of which are essentially variants of the one described by Assur (1960) and Weeks and Ackley (1986), the physical mechanism for the preferential elongation is not completely resolved. Under natural conditions and for larger pores, convective processes are likely to enhance enlargement of pores in the vertical direction (Niedrauer and Martin, 1979; Wettlaufer, 1998). To a lesser extent, migration of inclusions in a temperature gradient may also favour elongation of pores. The warming experiment in this study was conducted in the absence of macroscopic temperature gradients, however, with both the top and the bottom of the sample maintained at the same temperature (Fig. 1). The anisotropy in the ice lattice structure and the corresponding differences in free surface energy parallel and normal to the crystal c-axis can only explain significant shape anisotropy in the kinetically controlled regime of phase change, such as during the growth phase of sea ice (Weeks and Ackley, 1986; Wettlaufer, 1998). The equilibrium shape of brine inclusions, on the other hand, is dominated by the temperature-entropy term in the equation of state and hence, less susceptible to crystallographic lattice anisotropy.

This leaves another explanation that centers on the possibility that the presence of impurities in liquid or quasi-liquid form, in particular along grain and sub-grain boundaries, may be sufficient to foster invasion of these impurity-rich zones by brine during warming of the sample. If such proto-inclusions were to persist at lower temperatures they would provide pathways (possibly on a sub-pixel scale in the context of this MRI study) for an influx of brine upon warming to higher temperatures. In this context, the present work can only be the first step in elucidating the linkages between impurity content, microstructure and fluid flow in sea ice. MRI methods, in particular in conjunction with optical microscopy, appear to hold great promise in providing deeper insight into the thermal evolution of sea-ice fluid inclusions.

## 6. Summary and conclusions

MR imaging has been successfully applied to the high-resolution study of brine inclusions in sea ice. Samples were maintained at temperatures between −2°C and −25°C with the help of a flow-through cooling unit. At field gradients of 50 mT $m^{-1}$, the dielectric properties of brine with high loss factors at frequencies of few hundred MHz resulted in a significant degradation of the signal, heating of the sample due to high RF power and reduced image resolution (pixel sizes > 0.2 mm, slice thicknesses > 1 mm). These resolution problems, which had been encountered in earlier work, were overcome through the use of decane as a contrast agent and operation at higher gradients.

Analysis of MRI data of different types of artificial sea ice grown under controlled conditions in an environmental test basin and comparison with conventional thin-section image analysis indicates good to very good agreement between the two methods. Under optimal conditions, MRI data can be considered equivalent or superior to thin-section data at a comparable resolution (< 0.1-mm pixel size, slice thickness < 0.4 mm). Moreover, development of a segmentation technique based on the liquid fraction within each volume element allows for physically based, reliable discrimination between pores and ice matrix in the data sets.

Analysis of ice samples grown at zero and high under-ice current speeds reveal distinct differences in pore microstructure as a function of current speed. The lamellar microstructure of brine inclusions evident at zero current speeds is much less pronounced at current speeds of 0.16 m $s^{-1}$, with a correspond-

Proceedings of the 14th International Symposium on Ice, Potsdam, New York, USA, 27–31 July. A.A. Balkema, Rotterdam, pp. 363–370.

Eicken, H., Haas, C., Valero Delgado, F. Laboratory experiments on the dependence of sea-ice microstructure on the under-ice current speed, in preparation.

Eicken, H., Stierle, A., Bock, C., Miller, H., Junge, K., Krembs, C., Deming, J., 1999. Morphology and microphysics of sea-ice brine inclusions and their importance for fluid transport and microbial activity. Eos, Trans. Am. Geophys. Union 80, F36.

Freitag, J., 1999. The hydraulic properties of Arctic sea ice — implications for the small-scale particle transport (in German). Ber. Polarforsch. 325, 1–150.

Golden, K.M., Ackley, S.F., Lytle, V.I., 1998a. The percolation phase transition in sea ice. Science 282, 2238–2241.

Golden, K.M. et al., 1998b. Forward electromagnetic scattering models for sea ice. IEEE Trans. Geosci. Remote Sens. 36, 1655–1674.

Hallikainen, M., Winebrenner, D.P., 1992. The physical basis for sea ice remote sensing. In: Carsey, F.D. (Ed.), Microwave Remote Sensing of Sea Ice. Geophysical Monograph, vol. 68, American Geophysical Union, Washington, pp. 29–46.

Hannke, S., 1994. High-resolution density measurements on Arctic sea-ice cores with X-rays techniques (in German). Unpublished Undergraduate Thesis, University of Munich and Alfred Wegener Institute, Bremerhaven, Bremerhaven.

Junge, K., Krembs, C., Deming, J., Stierle, A., Eicken, H. A microscopic approach to investigate bacteria under in-situ conditions in sea-ice samples. Ann. Glaciol., 33, in press.

Kawamura, T., 1990. Nondestructive, three-dimensional density measurements of ice core samples by X-ray computed tomography. J. Geophys. Res. 95, 12407–12412.

Kawamura, T., 1988. Observations of the internal structure of sea ice by X-ray computed tomography. J. Geophys. Res. 93, 2343–2350.

Kovacs, A., Morey, R.M., Cox, G.F.N., Valleau, N.C., 1987. Electromagnetic property trends in sea ice: Part I. U.S.A. Cold Reg. Res. Eng. Lab., Hanover, NH CRREL Rep. 87-6:1-45.

Lange, M.A., 1988. Basic properties of Antarctic sea ice as revealed by textural analysis of ice cores. Ann. Glaciol. 10, 95–101.

Light, B., Maykut, G.A., 1999. Observations of sea-ice microstructure. Eos, Transact. Am. Geophys. Union 80, F222.

Lindquist, W.B., Lee, S.-M., Coker, D.A., Jones, K.W., Spanne, P., 1996. Medial axis analysis of void structure in three-dimensional tomographic images of porous media. J. Geophys. Res. 101, 8297–8310.

Melnichenko, N.A., Mikhaylov, V.I., Chizhik, V.I., 1979. Study of the temperature-dependence of the brine content in sea ice by the pulsed NMR method. Oceanology 19, 535–537.

Niedrauer, T.M., Martin, S., 1979. An experimental study of brine drainage and convection in young sea ice. J. Geophys. Res. 84, 1176–1186.

Perovich, D.K., 1998. Optical properties of sea ice. In: Leppäranta, M. (Ed.), Physics of Ice-Covered Seas, vol. 1. Univ. of Helsinki, Helsinki, pp. 195–230.

Perovich, D.K., Gow, A.J., 1996. Quantitative description of sea ice inclusions. J. Geophys. Res. 101, 18327–18343.

Rasband, W.S., Bright, D.S., 1995. NIH Image: a public domain image processing program for the Macintosh. J. Microbeam Analysis 4, 137–149.

Richardson, C., 1976. Phase relationships in sea ice as a function of temperature. J. Glaciol. 17, 507–519.

Richardson, C., Keller, E.E., 1966. The brine content of sea ice measured with a nuclear magnetic resonance spectrometer. J. Glaciol. 6, 89–100.

Schwarz, J., Frederking, R.M.W., Gavrilo, V.P., Petrov, I.G., Hirayama, K.-I., Mellor, M., Tryde, P., Vaudrey, K.D., 1981. Standardized testing methods for measuring mechanical properties of sea ice. Cold Reg. Sci. Technol. 4, 245–253.

Takashima, H., Yamakoshi, H., Maeda, T., Sakurai, A., 1992. Measurement of dielectric constant of model ice (Abstract). Proc. NIPR Symp. Polar Meteorol. Glaciol. 6, 160.

Underwood, E.E., 1970. Quantitative Stereology. Addison-Wesley, Reading, MA.

Weeks, W.F., 1998. Growth conditions and the structure and properties of sea ice. In: Leppäranta, M. (Ed.), Physics of Ice-Covered Seas, vol. 1, Univ. of Helsinki, Helsinki, pp. 25–104.

Weeks, W.F., Ackley, S.F., 1986. The growth, structure and properties of sea ice. In: Untersteiner, N. (Ed.), The Geophysics of Sea Ice. NATO ASI Ser., Ser B 146. Martinus Nijhoff Publ., Dordrecht, pp. 9–164.

Weeks, W.F., Gow, A.J., 1978. Preferred crystal orientations along the margins of the Arctic Ocean. J. Geophys. Res. 84, 5105–5121.

Wehrli, F.W., 1988. Principles of magnetic resonance. In: Stark, D.D., Bradley, W.G. (Eds.), Magnetic Resonance Imaging. Mosby Year Book, St. Louis. pp. 3–20.

Weissenberger, J., Dieckmann, G., Gradinger, R., Spindler, M., 1992. Sea ice: a cast technique to examine and analyze brine pockets and channel structure. Limnol. Oceanogr. 37, 179–183.

Wettlaufer, J., 1998. Introduction to crystallization phenomena in natural and artificial sea ice. In: Leppäranta, M. (Ed.), Physics of Ice-Covered Seas, vol. 1, Univ. of Helsinki, Helsinki, pp. 105–194.

ELSEVIER

# Magnetic resonance imaging of sea-ice pore fluids: methods and thermal evolution of pore microstructure

H. Eicken [a,*], C. Bock [b], R. Wittig [b], H. Miller [b], H.-O. Poertner [b]

[a] *Geophysical Institute, University of Alaska Fairbanks, P.O. Box 757320, Fairbanks, AK 99775-7320, USA*
[b] *Alfred Wegener Institute for Polar and Marine Research, P.O. Box 120161, D-27515 Bremerhaven, Germany*

## Abstract

Microstructure and thermal evolution of sea-ice brine inclusions were investigated with magnetic resonance imaging (MRI) techniques. Ice samples were kept at temperatures between $-2°C$ and $-25°C$ during $^1H$ imaging in a 4.7-T magnet at 200 MHz. Measurements were completed in a 20-cm diameter cylindrical probe and actively shielded gradient coils (max. 50 mT $m^{-1}$, pixel dimensions > 0.2 mm, slice thicknesses > 1 mm), and for higher resolution in a mini-imaging unit with a 9-cm diameter probe with gradient coils of 200 mT $m^{-1}$ (pixel dimensions < 0.1 mm, slice thickness < 0.4 mm). Absorption of radio-frequency (RF) signals in the dielectrically lossy brine resulted in degraded signals and was alleviated by use of a contrast agent (decane). MRI data and sea-ice thin section images agree very well (< 5% deviation for pore microstructural parameters). Analysis of ice grown under different current speeds indicates that pores are smaller and pore number densities larger at higher current speeds. The thermal evolution of fluid inclusions was studied on cold first-year ice samples, maintained at close to in-situ temperatures prior to experiments. Warming from $-21°C$ to $-10°C$ to $-6°C$ is associated with a distinct increase in pore size (from 1.5 to 1.7 to 2.6 mm for the upper 10-percentile in the vertical) and elongation (4.0 to 4.2 to 6.2 for ratio of major to minor pore axes in the vertical) and a decrease in number densities (0.75 to 0.62 to 0.58 mm$^{-3}$ in the vertical). Aspect ratios increased from 4:2:1 to 6:2:1 (upper 10-percentile), indicating expansion and merging of pores in the vertical, possibly promoted by microscopic residual brine inclusions. © 2000 Elsevier Science B.V. All rights reserved.

*Keywords:* Sea ice; Nuclear magnetic resonance; Pore structure; Crystal growth; Chukchi Sea; Image analysis

## 1. Introduction

Sea ice is distinct from other types of ice present at the earth's surface owing to the ubiquitous occurrence of sub-millimeter to decimeter-sized inclusions of liquid brine (Weeks and Ackley, 1986; Weeks, 1998; Wettlaufer, 1998). These inclusions strongly affect radiative and heat transfer through the ice (Perovich, 1998; Weeks, 1998) and they control the electromagnetic properties of sea ice (Hallikainen and Winebrenner, 1992; Golden et al., 1998a,b). As the brine seeks to maintain thermodynamic equilibrium with the ice matrix, the morphology and size of the inclusions depends strongly on the salinity and

* Corresponding author. Fax: +1-907-474-7290.
 *E-mail address:* hajo.eicken@gi.alaska.edu (H. Eicken).

have been maintained at the in-situ temperature after sampling. The ice samples originate both from ice-tank experiments devoted to the study of microstructural evolution (Eicken et al., 1998) as well as from coastal sea ice obtained at Barrow in northern Alaska. Apart from a discussion of methodological aspects, the evolution of pore microstructure will receive particular attention in the context of ice permeability and fluid transport at lower temperatures (Golden et al., 1998a,b; Freitag, 1999), as the present contribution is part of a study devoted to fluid transport and its importance for survival of microorganisms within sea-ice pores at low temperatures (Eicken et al., 1999; Deming and Huston, in press; Junge et al., in press).

## 2. Methods

### 2.1. Principles and instrumentation of MRI

The detection of water within a multi-phase system with nuclear magnetic resonance (NMR) techniques is a well-established technique and among other topics has also been applied to problems in sea-ice research to study the thermal evolution of the brine fraction in sea ice (Richardson and Keller, 1966; Richardson, 1976; Melnichenko et al., 1979). MRI is based on the principle that the resonance frequency depends on the position of a nucleus in a magnetic field gradient (Wehrli, 1988; Callaghan, 1991). The frequency spectrum obtained over a sample volume can then be decomposed into individual frequencies (containing information about the $x$–$y$ position) and amplitudes (containing information about the spin, or in the case of $^1$H, proton density). Image acquisition and in particular the spatial resolution are determined by the timing and characteristics of the RF pulses as well as the magnitude of the field gradient across the sample volume.

The present study has been carried out in a Bruker Biospec 47/40 imaging spectrometer (Bruker, Ettlingen, Germany), at 4.7 T (Larmor frequency for $^1$H = 200 MHz) equipped with actively shielded gradient coils providing field gradients of 50 mT m$^{-1}$ and a mini-imaging unit with gradient field strength of up to 200 mT m$^{-1}$. Cylindrical probes adapted to

high-conductivity samples were used for RF signal transmission and detection (20- and 9-cm diameter. respectively). Image acquisition was mostly confined to a spin–echo method (multi-slice multi-echo. MSME, matrix size up to $1024 \times 512$, field-of-view (FOV) up to $12 \times 12$ cm (standard imaging, S) or $6 \times 6$ cm (mini imaging, M), slice thickness down to 1.2 mm (S) or 0.3 mm (M), slice separation down to 5 mm (S) or 2 mm (M), with sinc3 RF pulses of 3000-$\mu$s duration) or a gradient–echo method (FLASH, flip angle 22.5°, sinc3 of 3000 $\mu$s) with typical echo times TE of 17.5 ms for MSME and 5 ms for FLASH. Repetition time TR was on the order of 300–2000 ms for MSME and 400–500 ms for FLASH. Typically, measurements for individual samples lasted between 4 and 12 h, averaging over up to eight samples in order to increase the signal-to-noise ratio (SNR).

### 2.2. Samples and sample preparation

In order to optimize MRI system performance and to develop and improve upon methods of MRI data analysis, a first set of measurements was carried out on artificial sea ice grown under fully controlled environmental conditions. These samples originated from ice-growth experiments in the Environmental Arctic Test Basin (EATB) of the Hamburgische Schiffbauversuchsanstalt in 1996 and 1997 (INTERICE I, Eicken et al., 1998). In a basin of dimensions $30 \times 6 \times 1.2$ m, a congelation-type sea-ice sheet was grown from artificial seawater, prepared by dissolving Aquarium Systems "Instant Ocean" artificial seasalt in tapwater, to between 0.15- and 0.2-m thickness (for details, see Eicken et al., 1998). The resulting ice is representative of new ice grown under natural conditions and exhibits the same inventory of small- and large-scale pore features (Cottier et al., 1999; Eicken et al., in preparation).

Samples for the studies of sea-ice thermal evolution were obtained in March 1999 from the fast-ice cover near Barrow (sampling location at 71°19.95′N 156°40.55′W), on the northern coast of Alaska. Numerous studies of the ice cover at this location have shown it to be representative of homogeneous first-year, undeformed Arctic congelation-type sea ice (Weeks and Gow, 1978; Cole and Shapiro, 1998). At

physical properties and microstructure of the sample. Given the lack of sea-ice MRI work, a first step in the present study consisted of an optimization of the instrumental parameters. Analysis of ice samples immersed in brine at the respective in-situ temperatures established that the SNR of gradient–echo FLASH images was poor, most likely due to RF loss in the brine, and that the images showed artifacts due to susceptibility changes within the ice matrix (resulting from air bubbles, brine–ice transitions, eddy currents). Spin–echo images yielded results that were not severely compromised by artifacts due to eddy currents induced in the brine layer surrounding the sample (5- to 10-mm thick, see bottom of Fig. 2).
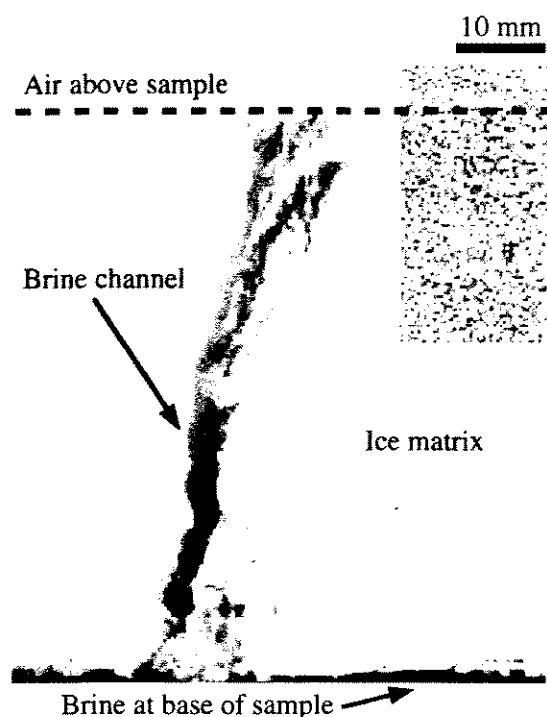


Fig. 2. MRI cross-section through layer of artificial sea ice (sample H961219Q, 0.07- to 0.14-m depth, slice thickness 1.5 mm, pixel size 0.4×0.4 mm) recorded in immersion of artificial brine at −2°C with a spin–echo method (MSME). Note that here and in all subsequent images, MRI and thin-section scenes are shown as inverted contrast images (pores appearing dark). While the brine channel in the center is well discernible, very few pore features can be identified in the ice matrix, as is evident from the subregion in the upper right that has been subjected to a linear histogram transform to enhance the contrast in the ice matrix.

However, due to the higher RF power input (90°–180° flip angles) in comparison to FLASH, the probe was heating up at in-situ temperatures, compromising long-term image sampling. As apparent from the vertical cross-section through a new-ice cover shown in Fig. 2, the structure of brine channels and other larger pore features is well-resolved. This includes the upper layers of the sample where the channel is widened and to some extent branched out. As shown by the contrast-enhanced inset in Fig. 2, there is no discernible difference in the signal between ice matrix and overlying air. At a pixel size of approximately 0.4 mm and a slice thickness of 1.5 mm, smaller brine inclusions are not distinguishable within the ice matrix.

While the resolution of the imaging system as defined by the size of the volume elements (voxels) may not allow for direct discrimination of small-scale pores, it can still be feasible to derive the fraction of such fluid inclusions based on the signal strength integrated over a larger sample sub-volume. Based on Callaghan (1991), the SNR for a signal induced in the receiver coils of radius $r$ during resonance at frequency $f_0$ and for a frequency bandwidth $\Delta f$ is directly proportional to the volume fraction $N_p$ of protons (in this case $^1$H in the brine) in a subvolume $V_s$ such that

$$\text{SNR} \approx K \frac{N_p V_s f_0^{7/4}}{r \Delta f^{1/2}} \tag{1}$$

with constant $K = 1.2 \times 10^{-3}$ s$^{5/4}$ m$^{-2}$ based on instrument parameters and assuming solenoidal coils at room temperature. For a voxel volume of (0.4 mm)$^3$ and parameters characteristic of the Bruker system employed in this study, SNR is roughly 100 in order of magnitude, with values decreasing to below 10 as higher resolutions are approached. In solids, the signal is broadened over a wider resonance frequency band. In combination with shorter relaxation times this allows for a direct discrimination between brine and ice, with the signal for pure ice and air being close to indistinguishable (Fig. 2, Table 1). Disregarding the submicroscopic effects on the relaxation of $^1$H along phase boundaries, the liquid fraction $f_s$ in a given sample volume with a signal of magnitude $S$ can be derived through a set
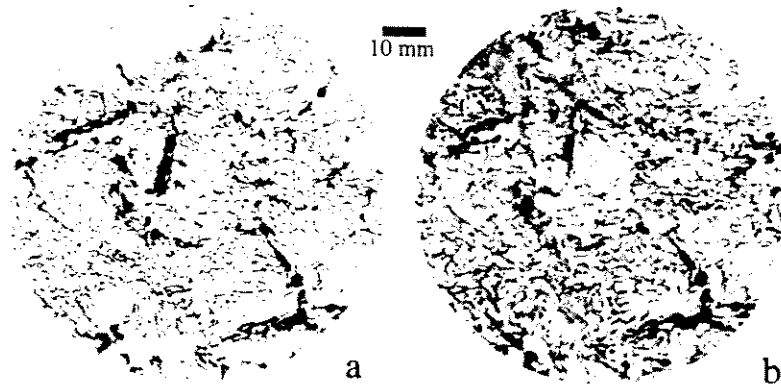
Fig. 3. Comparison of pore microstructure between horizontal thin-section image (a) and MRI data (b) of the same sea-ice sample (H961219Q, 0.05-m depth). Pores appear dark in both images, with both larger secondary brine channels and pockets as well as smaller brine layers discernible. Pore-free areas along margin of upper half of thin-section sample are artifacts due to sample processing (see Table 2 for further details on image acquisition and data).

ton density as well as its immiscibility with water. In this way, spin–echo imaging could be performed with greater matrix sizes to increase resolution, more adequate and shorter pulses resulting in thinner slice thicknesses, and a larger number of signal averages to increase SNR. At the same time, RF heating was significantly reduced due to better probe matching and reduction in eddy currents, allowing for longer measurement periods. Fig. 3 demonstrates that samples saturated with decane resulted in a significant improvement of image quality. Moreover, increased signal strength allowed for a reduction in the linear voxel dimensions by more than half (see instrument parameters shown in Table 2). Thus, in a standard mode of operation with a field gradient of 50 mT

$m^{-1}$ in the 20-cm-diameter resonator, the method appears to sufficiently resolve both larger-scale pores such as brine channels as well as the sub-millimeter brine layers characteristic of columnar sea ice (Fig. 3).

### 3.2. Segmentation of MRI data

Quantitative microstructural analysis requires the segmentation of MRI data into solid ice and fluid inclusions. In the case of MRI this can be approached in a rigorous fashion, given that the signal is proportional to the total number of liquid-phase protons in a given sub-volume. Hence, the signal associated with the pure end-member components $S_s$ and $S_l$ (ice and brine or decane) can be employed to constrain Eq. (2) and allow for the derivation of the liquid volume fraction (i.e., porosity) of individual volume elements. $S_s$ and $S_l$ can be derived either manually through measurement over a test volume or from a sample histogram such as the one shown in Fig. 4. With the liquid volume fraction computed from the signal of each individual voxel according to Eq. (2), the segmentation criterion can be based on a simple fractional-volume threshold, with all voxels corresponding to a liquid volume fraction $f_l \leq 0.5$ classified as ice and all those with $f_l > 0.5$ as pores. The classification error due to a finite SNR can then be derived from the FOV and the number of samples averaged for each data set (see Section 5.1).

Table 2

Comparison between thin-section image and MRI data (sample H961219Q, 0.05-m depth, low-resolution standard gradient coils, see Fig. 3)

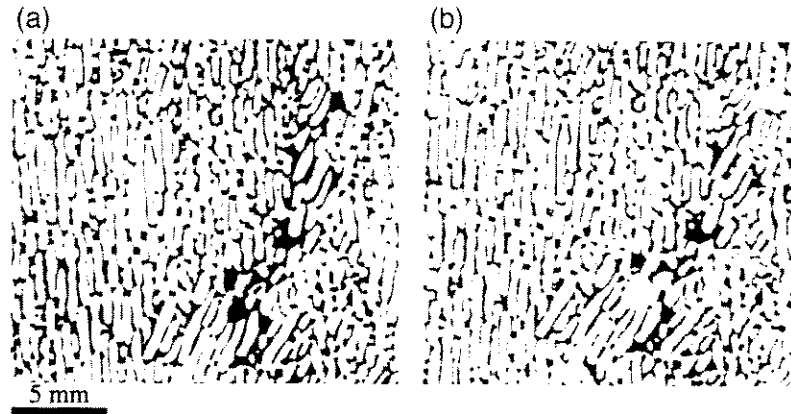| Parameter | Thin section data | MRI data |
|---|---|---|
| | Mean ± $\sigma$ | Mean ± $\sigma$ |
| Pixel size (horizontal), mm | 0.18 | 0.21 |
| Slice thickness (vertical), mm | < 0.05 | 1.26 |
| Porosity | 0.187 | 0.176 |
| Pore area, mm$^2$ | 0.76 ± 3.40 | 1.10 ± 4.40 |
| Pore perimeter, mm | 3.34 ± 7.40 | 3.97 ± 8.60 |
| Pore major axis, mm | 1.06 ± 1.23 | 1.19 ± 1.44 |
| Pore minor axis, mm | 0.45 ± 0.44 | 0.58 ± 0.56 |

Fig. 6. Comparison of pore microstructure between horizontal thin-section image (a) — averaged over three serial sections spaced 0.2 mm apart — and MRI data recorded with the mini-imaging unit (b) of the same sea-ice sample (H970128Q, 0.15-m depth). Pores appear dark in both images, with system of subparallel brine layers clearly discernible (see Table 3 for further details on image acquisition and pore-size data).

Ackley, 1986). With an FOV extending over close to 100 mm, a pixel resolution of around 0.2 mm and a slice thickness of $> 1$ mm (Table 2), imaging in a field gradient of 50 mT m$^{-1}$ is ideal for studies of pore macrostructure in a larger sample volume (Figs. 2 and 3), but proved only marginally effective at properly resolving the sub-millimeter pore structure. This is also borne out by the mismatch apparent between thin-section and MRI data at smaller pore sizes in Fig. 5.

A significant increase in resolution and data quality has been achieved, however, by imaging in higher field gradients of up to 200 mT m$^{-1}$. In combination with the cooling chamber, this system allows for the

analysis of samples with approximate dimensions $30 \times 30 \times 60$ mm, comparable to high-resolution image analysis of thin sections. While the smaller FOV reduces the SNR, this can be compensated for by longer integration times. Smaller sample sizes also reduce the amount of attenuation of the RF signal

Table 3

Comparison between thin-section image and MRI data (sample H970128Q, 0.15-m depth, high-resolution, 200 mT m$^{-1}$ gradient coils, see Fig. 6)

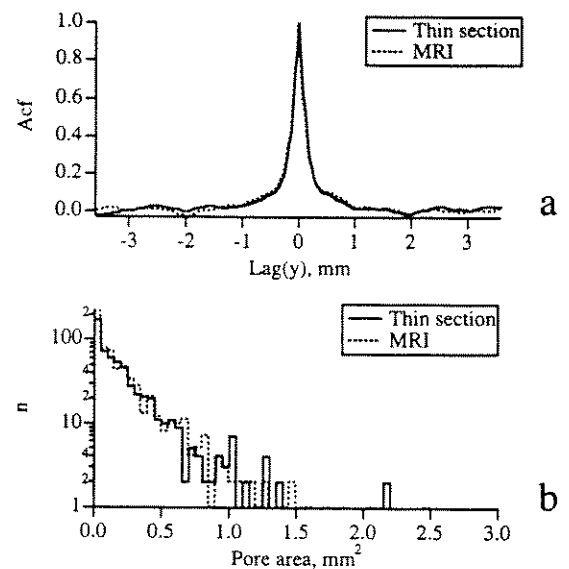| Parameter | Thin section data | MRI data |
|---|---|---|
| | Mean $\pm \sigma$ | Mean $\pm \sigma$ |
| Pixel size (horizontal), mm | 0.08 | 0.09 |
| Slice thickness (vertical), mm | $< 0.05$ | 0.4 |
| Porosity | 0.175 | 0.181 |
| Pore area, mm$^2$ | $0.32 \pm 1.31$ | $0.28 \pm 0.66$ |
| Pore perimeter, mm | $2.92 \pm 5.80$ | $2.72 \pm 3.93$ |
| Pore major axis, mm | $0.87 \pm 0.90$ | $0.85 \pm 0.82$ |
| Pore minor axis, mm | $0.30 \pm 0.23$ | $0.29 \pm 0.22$ |



Fig. 7. Comparison of microstructural parameters for thin-section and MRI images shown in Fig. 6 (sample H970128Q, 0.15-m depth). Vertical cross-section through 2-D acf (Fig. 7a) and pore-size distribution based on cross-sectional pore area (Fig. 7b).

Table 4

Comparison between MRI data (horizontal and vertical sections) for ice grown at different under-ice current speeds (high-resolution imaging at 200 mT m$^{-1}$, see Figs. 8 and 9; mean and standard deviation for mean values of eight individual sections per sample are shown)

| Parameter | H970128Q, 0.15 m | | H961219C, 0.08 m | |
|---|---|---|---|---|
| | Horizontal | Vertical | Horizontal | Vertical |
| Current velocity, m s$^{-1}$ | 0.00 | 0.00 | 0.16 | 0.16 |
| Porosity | $0.21 \pm 0.01$ | $0.20 \pm 0.02$ | $0.11 \pm 0.01$ | $0.11 \pm 0.01$ |
| Pore area, mm$^2$ | $0.27 \pm 0.03$ | $0.43 \pm 0.10$ | $0.14 \pm 0.02$ | $0.25 \pm 0.04$ |
| Pore perimeter, mm | $2.66 \pm 0.26$ | $2.94 \pm 0.47$ | $1.43 \pm 0.11$ | $1.95 \pm 0.15$ |
| Pore major axis $a_{maj}$, mm | $0.83 \pm 0.06$ | $0.87 \pm 0.13$ | $0.50 \pm 0.03$ | $0.68 \pm 0.03$ |
| Pore minor axis $a_{min}$, mm | $0.30 \pm 0.02$ | $0.30 \pm 0.03$ | $0.24 \pm 0.01$ | $0.25 \pm 0.01$ |

tions with an under-ice current speed of approximately 0.16 m s$^{-1}$. These measurements are motivated by the lack of data and understanding of the microstructural evolution of sea ice in different hydrodynamic regimes in particular as it relates to pore structure and ice properties. Changes in the microstructural evolution are forced by variability in the thickness and structure of the laminar boundary layer, on the order of a few millimeters thick, ahead of the advancing ice–water interface (Weeks and Ackley, 1986; Wettlaufer, 1998). The MRI data presented here are complementary to a more detailed study of the evolution of pore space as a function of under-ice current speed based mostly on horizontal thin-section data by Eicken et al. (in preparation).

A comparison between the image data shown for an ice cover grown at zero current (Fig. 8) and at an under-ice current speed of approximately 0.16 m s$^{-1}$ (Fig. 9), in the upper range of natural conditions (McPhee, 1990), demonstrates strong contrasts in microstructure. For ice affected by a current of this magnitude, the grain substructure with parallel or sub-parallel brine layers separated by orderly arrays of ice lamellae (Fig. 8a) breaks down into smaller disjoint pores of more isometric cross-section (Fig. 9a). In the vertical plane (Figs. 8b and 9b), this structural change is just as pronounced with the parallel brine layer arrays replaced by shorter (Fig. 9c), less well-ordered brine tubes. Such changes evident in the MRI scenes are reflected in the pore-
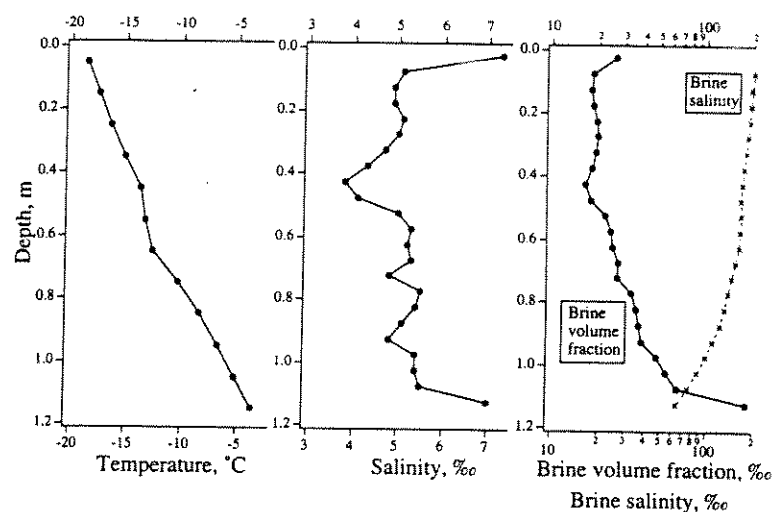
Fig. 10. Profiles of temperature (left), salinity (center) as well as brine volume fraction and brine salinity (right, derived based on phase relations according to Cox and Weeks, 1983) through the fast-ice sheet at the sampling site near Barrow in the Chukchi Sea (March 12, 1999).

fluid inclusions cannot be arrived at in such a fashion, however. The few observations of changes in pore structure are either based on semi-quantitative microscopy (Assur, 1960) or measurements carried out on larger populations of samples (Perovich and Gow, 1996).

Here, we have studied changes in pore microstructure associated with a warming from below −21°C to −6°C throughout the same, undisturbed ice sample volume. Samples had been obtained from the coastal fast-ice cover in the eastern Chukchi Sea near Barrow during the coldest weeks of the year (Section 2.2). Temperatures were maintained at or close to the in-situ temperature which approached −20°C in the upper ice layers (Fig. 10) up to the start of the MRI analysis. Salinity measurements and microstructural studies performed on additional ice cores obtained at the study site indicate the ice cover to consist of prototypical first-year columnar, congelation-type sea ice with a C-shaped salinity profile

(Figs. 10 and 11), which is in agreement with earlier studies carried out at this location (Weeks and Gow, 1978; Cole and Shapiro, 1998). The MRI sample was obtained from the cold, uppermost layers of columnar ice, composed of smaller crystals and lacking the preferred azimuthal alignment of crystallographic c-axes displayed at greater depths (Fig. 11). Based on the salinity and temperature measurements, the brine volume fraction in the upper layers of columnar sea ice is approximately 20‰ (Fig. 10, derived according to Cox and Weeks, 1983). The corresponding MRI data shown in Fig. 12 and Table 5 are in fair agreement with this bulk brine porosity.

The most interesting aspects of Fig. 12, however, are the changes in pore microstructure associated with a warming of the sample from −21°C to −6°C. As is clearly evident, pores present at low temperatures enlarge and join, while at the same time new populations of pores appear in the image data (see Table 5, pore number densities). The latter are

Table 5

Thermal evolution of pore microstructural parameters as derived from MRI data for sample CS990312, 0.10- to 0.13-m depth (bold numbers in upper rows are mean values, standard deviation indicated in lower rows)

| $T$ (°C) | Vertical sections | | | Horizontal sections | | | $P$ | $N_{P,ver}$ (mm$^{-3}$) | $N_{P,hor}$ (mm$^{-3}$) |
|---|---|---|---|---|---|---|---|---|---|
| | $a_{maj}$ (mm) | $a_{min}$ (mm) | $r_{maj/min}$ | $a_{maj}$ (mm) | $a_{min}$ (mm) | $r_{maj/min}$ | | | |
| *Entire data set* | | | | | | | | | |
| **−21** | **0.42** | **0.21** | **1.73** | **0.34** | **0.22** | **1.49** | **0.026** | **0.75** | **0.95** |
| | 0.47 | 0.10 | 1.10 | 0.19 | 0.09 | 0.56 | | | |
| *Top 10 percentile* | | | | | | | | | |
| **−21** | **1.53** | **0.40** | **3.96** · | **0.75** | **0.37** | **2.16** | | | |
| | 0.70 | 0.11 | 1.61 | 0.23 | 0.10 | 0.87 | | | |
| *Entire data set* | | | | | | | | | |
| **−10** | **0.43** | **0.22** | **1.73** | **0.34** | **0.23** | **1.46** | **0.027** | **0.62** | **1.05** |
| | 0.52 | 0.10 | 1.18 | 0.22 | 0.10 | 0.57 | | | |
| *Top 10 percentile* | | | | | | | | | |
| **−10** | **1.66** | **0.40** | **4.20** | **0.81** | **0.39** | **2.19** | | | |
| | 0.83 | 0.10 | 1.89 | 0.33 | 0.10 | 0.88 | | | |
| *Entire data set* | | | | | | | | | |
| **−6** | **0.70** | **0.26** | **2.32** | **0.38** | **0.25** | **1.53** | **0.038** | **0.58** | **1.08** |
| | 0.79 | 0.13 | 1.74 | 0.24 | 0.11 | 0.59 | | | |
| *Top 10 percentile* | | | | | | | | | |
| **−6** | **2.62** | **0.45** | **6.16** | **0.92** | **0.42** | **2.32** | | | |
| | 1.06 | 0.15 | 2.37 | 0.34 | 0.12 | 0.84 | | | |

$a_{maj}$, $a_{min}$: major and minor axis of inscribed ellipse, $r_{maj/min}$: ratio between major and minor axis. $P$: porosity, $N_{P,ver}$, $N_{P,hor}$: number density of pores.

incident light, is the slice thickness, which may be larger than the characteristic pore dimension. Slice thicknesses for MRI data measured with the standard gradient coils are generally larger than 1 mm (depending on matrix size, FOV and available RF power) and even a data set optimized for resolution is likely to have slice thicknesses larger than 0.3 mm. This introduces stereological effects (Underwood, 1970; Eicken, 1993) that affect the apparent pore size and to a lesser extent, for columnar sea ice, the apparent shape of the inclusions.

The close spacing between individual slices, such as a set of eight separated by approximately 4 mm each for the samples shown in Figs. 8 and 9, allows an assessment of the spatial variability of pore volume and microstructure at a very small scale. The standard deviation of the slice porosities varies between 7% and 12% for these two different samples (Table 4), with maximum deviations of 20%, corresponding to maximum bulk salinity differences of approximately 1.4‰ salinity. Microstructural size parameters also exhibit standard deviations of 5–10% between sets of horizontal or vertical slices. These fluctuations are most likely associated with grain-boundaries and other microstructural discontinuities in the sample.

### 5.2. The thermal evolution of sea-ice pore space

In contrast with destructive imaging techniques such as standard thin-section processing, MRI can provide imagery of a larger sea-ice sample as it undergoes temperature changes. Here, these changes have been documented for a sample of columnar ice maintained close to in-situ temperatures after coring and then warmed from $-21°C$ to $-6°C$. As shown in Fig. 12 and Table 5 and summarized in Fig. 13, warming was accompanied by significant microstructural changes, in particular between $-10°C$ and $-6°C$. Concurrently, pore volumes increased by approximately 50%, which is in good agreement with theoretical estimates based on the ice salinity and thermodynamic phase relations (Fig. 13). As expected, based on earlier semi-quantitative observations on thin sections (Assur, 1960, Weeks and Ackley, 1986), the vertical elongation of pores increases as a result of warming, with the ratio between major and minor axis (inscribed ellipse)
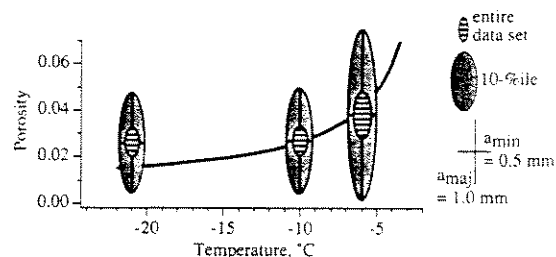


Fig. 13. Thermal evolution of fluid inclusions for Chukchi Sea ice sample (CS990312, 0.13- to 0.16-m depth, see Fig. 10 for profile properties and Fig. 11 for thin-section images) based on MRI data. The relative proportions of the major and minor pore axis dimensions are shown for the entire data set and the upper 10-percentile (scale shown at right). The solid line denotes the increase in brine porosity based on sample bulk salinity and phase relations.

$r_{maj/min}$ increasing from 4 to more than 6 for the upper 10-percentile of pores in a sample. During the same temperature interval, $r_{maj/min}$ increased by less than 10% to 2.3% for the upper 10-percentile in horizontal MRI slices. Based on the mean parameters, the aspect ratios of brine inclusions in three dimensions (vertical, horizontal parallel to crystal basal layer, horizontal perpendicular to basal layer) have thus been observed to increase from 1.9:1.5:1 to 2.8:1.5:1 for the entire pore population and from 4.1:2.0:1 to 6.2:2.2:1 for the upper 10-percentile.

With increasing size, pores have been observed to merge and coalesce (Fig. 14). While this circumstance is also reflected in a decrease in the number density of pores $N_p$ in vertical MRI slices, the appearance of new populations of small pores in the image data has diminished the overall magnitude of this effect. Fig. 14 illustrates the problem and also shows that the assessment of pore morphology (e.g., $r_{maj/min}$) is to some extent compromised as well. Thus, the merging of four apparently isolated pores into a large, tubular inclusion in the center is accompanied by the "appearance" of new pores to the right and above this major feature. The latter are responsible for an increase in $N_p$ for this small sub-scene. In the horizontal MRI slices, this process is believed to be responsible for the slight increase observed for $N_{p,hor}$ with increasing temperature (Table 5). A similar, and upon first reflection counter-intuitive trend was reported by Perovich and Gow (1996) in their analysis of thin-section images of warming ice sam-

Finally, the issue of resolution also affects interpretation of MRI data in the context of pore connectivity and fluid transport. Thus, the interpretation of the merging of individual pores discussed above and shown in Fig. 14 only applies to pore connections visible at the smallest scale resolved in the data set. At sub-pixel scales, the set of pores barely discernible at −21°C in Fig. 14 may already have been linked through smaller-scale vein networks. Given some of the limitations of both MRI and ordinary thin-section analysis, we suspect that only true microscopic analysis may provide deeper insight into this problem. The relevance of this question far exceeds the merely technical aspects of microstructural analysis, however. While the finding that pores are preferentially elongating and in particular merging in the vertical direction is compatible with classical sea-ice pore microstructural models, all of which are essentially variants of the one described by Assur (1960) and Weeks and Ackley (1986), the physical mechanism for the preferential elongation is not completely resolved. Under natural conditions and for larger pores, convective processes are likely to enhance enlargement of pores in the vertical direction (Niedrauer and Martin, 1979; Wettlaufer, 1998). To a lesser extent, migration of inclusions in a temperature gradient may also favour elongation of pores. The warming experiment in this study was conducted in the absence of macroscopic temperature gradients, however, with both the top and the bottom of the sample maintained at the same temperature (Fig. 1). The anisotropy in the ice lattice structure and the corresponding differences in free surface energy parallel and normal to the crystal c-axis can only explain significant shape anisotropy in the kinetically controlled regime of phase change, such as during the growth phase of sea ice (Weeks and Ackley, 1986; Wettlaufer, 1998). The equilibrium shape of brine inclusions, on the other hand, is dominated by the temperature-entropy term in the equation of state and hence, less susceptible to crystallographic lattice anisotropy.

This leaves another explanation that centers on the possibility that the presence of impurities in liquid or quasi-liquid form, in particular along grain and sub-grain boundaries, may be sufficient to foster invasion of these impurity-rich zones by brine during warming of the sample. If such proto-inclusions were to persist at lower temperatures they would provide pathways (possibly on a sub-pixel scale in the context of this MRI study) for an influx of brine upon warming to higher temperatures. In this context, the present work can only be the first step in elucidating the linkages between impurity content, microstructure and fluid flow in sea ice. MRI methods, in particular in conjunction with optical microscopy, appear to hold great promise in providing deeper insight into the thermal evolution of sea-ice fluid inclusions.

## 6. Summary and conclusions

MR imaging has been successfully applied to the high-resolution study of brine inclusions in sea ice. Samples were maintained at temperatures between −2°C and −25°C with the help of a flow-through cooling unit. At field gradients of 50 mT m⁻¹, the dielectric properties of brine with high loss factors at frequencies of few hundred MHz resulted in a significant degradation of the signal, heating of the sample due to high RF power and reduced image resolution (pixel sizes > 0.2 mm, slice thicknesses > 1 mm). These resolution problems, which had been encountered in earlier work, were overcome through the use of decane as a contrast agent and operation at higher gradients.

Analysis of MRI data of different types of artificial sea ice grown under controlled conditions in an environmental test basin and comparison with conventional thin-section image analysis indicates good to very good agreement between the two methods. Under optimal conditions, MRI data can be considered equivalent or superior to thin-section data at a comparable resolution ( < 0.1-mm pixel size, slice thickness < 0.4 mm). Moreover, development of a segmentation technique based on the liquid fraction within each volume element allows for physically based, reliable discrimination between pores and ice matrix in the data sets.

Analysis of ice samples grown at zero and high under-ice current speeds reveal distinct differences in pore microstructure as a function of current speed. The lamellar microstructure of brine inclusions evident at zero current speeds is much less pronounced at current speeds of 0.16 m s⁻¹, with a correspond-

Proceedings of the 14th International Symposium on Ice, Potsdam, New York, USA, 27–31 July. A.A. Balkema, Rotterdam, pp. 363–370.

Eicken, H., Haas, C., Valero Delgado, F. Laboratory experiments on the dependence of sea-ice microstructure on the under-ice current speed, in preparation.

Eicken, H., Stierle, A., Bock, C., Miller, H., Junge, K., Krembs, C., Deming, J., 1999. Morphology and microphysics of sea-ice brine inclusions and their importance for fluid transport and microbial activity. Eos, Trans. Am. Geophys. Union 80, F36.

Freitag, J., 1999. The hydraulic properties of Arctic sea ice — implications for the small-scale particle transport (in German). Ber. Polarforsch. 325, 1–150.

Golden, K.M., Ackley, S.F., Lytle, V.I., 1998a. The percolation phase transition in sea ice. Science 282, 2238–2241.

Golden, K.M. et al., 1998b. Forward electromagnetic scattering models for sea ice. IEEE Trans. Geosci. Remote Sens. 36, 1655–1674.

Hallikainen, M., Winebrenner, D.P., 1992. The physical basis for sea ice remote sensing. In: Carsey, F.D. (Ed.), Microwave Remote Sensing of Sea Ice. Geophysical Monograph, vol. 68, American Geophysical Union, Washington, pp. 29–46.

Hannke, S., 1994. High-resolution density measurements on Arctic sea-ice cores with X-rays techniques (in German). Unpublished Undergraduate Thesis, University of Munich and Alfred Wegener Institute, Bremerhaven, Bremerhaven.

Junge, K., Krembs, C., Deming, J., Stierle, A., Eicken, H. A microscopic approach to investigate bacteria under in-situ conditions in sea-ice samples. Ann. Glaciol., 33, in press.

Kawamura, T., 1990. Nondestructive, three-dimensional density measurements of ice core samples by X-ray computed tomography. J. Geophys. Res. 95, 12407–12412.

Kawamura, T., 1988. Observations of the internal structure of sea ice by X-ray computed tomography. J. Geophys. Res. 93, 2343–2350.

Kovacs, A., Morey, R.M., Cox, G.F.N., Valleau, N.C., 1987. Electromagnetic property trends in sea ice: Part I. U.S.A. Cold Reg. Res. Eng. Lab., Hanover, NH CRREL Rep. 87-6:1–45.

Lange, M.A., 1988. Basic properties of Antarctic sea ice as revealed by textural analysis of ice cores. Ann. Glaciol. 10, 95–101.

Light, B., Maykut, G.A., 1999. Observations of sea-ice microstructure. Eos, Transact. Am. Geophys. Union 80, F222.

Lindquist, W.B., Lee, S.-M., Coker, D.A., Jones, K.W., Spanne, P., 1996. Medial axis analysis of void structure in three-dimensional tomographic images of porous media. J. Geophys. Res. 101, 8297–8310.

Melnichenko, N.A., Mikhaylov, V.I., Chizhik, V.I., 1979. Study of the temperature-dependence of the brine content in sea ice by the pulsed NMR method. Oceanology 19, 535–537.

Niedrauer, T.M., Martin, S., 1979. An experimental study of brine drainage and convection in young sea ice. J. Geophys. Res. 84, 1176–1186.

Perovich, D.K., 1998. Optical properties of sea ice. In: Lepparanta, M. (Ed.), Physics of Ice-Covered Seas, vol. 1. Univ. of Helsinki, Helsinki, pp. 195–230.

Perovich, D.K., Gow, A.J., 1996. Quantitative description of sea ice inclusions. J. Geophys. Res. 101, 18327–18343.

Rasband, W.S., Bright, D.S., 1995. NIH Image: a public domain image processing program for the Macintosh. J. Microbeam Analysis 4, 137–149.

Richardson, C., 1976. Phase relationships in sea ice as a function of temperature. J. Glaciol. 17, 507–519.

Richardson, C., Keller, E.E., 1966. The brine content of sea ice measured with a nuclear magnetic resonance spectrometer. J. Glaciol. 6, 89–100.

Schwarz, J., Frederking, R.M.W., Gavrilo, V.P., Petrov, I.G., Hirayama, K.-I., Mellor, M., Tryde, P., Vaudrey, K.D., 1981. Standardized testing methods for measuring mechanical properties of sea ice. Cold Reg. Sci. Technol. 4, 245–253.

Takashima, H., Yamakoshi, H., Maeda, T., Sakurai, A., 1992. Measurement of dielectric constant of model ice (Abstract). Proc. NIPR Symp. Polar Meteorol. Glaciol. 6, 160.

Underwood, E.E., 1970. Quantitative Stereology. Addison-Wesley, Reading, MA.

Weeks, W.F., 1998. Growth conditions and the structure and properties of sea ice. In: Lepparanta, M. (Ed.), Physics of Ice-Covered Seas, vol. 1, Univ. of Helsinki, Helsinki, pp. 25–104.

Weeks, W.F., Ackley, S.F., 1986. The growth, structure and properties of sea ice. In: Untersteiner, N. (Ed.), The Geophysics of Sea Ice. NATO ASI Ser., Ser B 146. Martinus Nijhoff Publ., Dordrecht, pp. 9–164.

Weeks, W.F., Gow, A.J., 1978. Preferred crystal orientations along the margins of the Arctic Ocean. J. Geophys. Res. 84, 5105–5121.

Wehrli, F.W., 1988. Principles of magnetic resonance. In: Stark, D.D., Bradley, W.G. (Eds.), Magnetic Resonance Imaging. Mosby Year Book, St. Louis, pp. 3–20.

Weissenberger, J., Dieckmann, G., Gradinger, R., Spindler, M., 1992. Sea ice: a cast technique to examine and analyze brine pockets and channel structure. Limnol. Oceanogr. 37, 179–183.

Wettlaufer, J., 1998. Introduction to crystallization phenomena in natural and artificial sea ice. In: Lepparanta, M. (Ed.), Physics of Ice-Covered Seas, vol. 1, Univ. of Helsinki, Helsinki, pp. 105–194.